
TRANSFERRING VISUAL EXPLAINABILITY OF SELF-EXPLAINING MODELS TO PREDICTION-ONLY MODELS WITHOUT ADDITIONAL TRAINING

A PREPRINT

Yuya Yoshikawa
STAIR Lab, Chiba Institute of Technology
yoshikawa@stair.center

Ryotaro Shimizu
ZOZO Research
ryotaro.shimizu@zozo.com

Takahiro Kawashima
ZOZO Research
takahiro.kawashima@zozo.com

Yuki Saito
ZOZO Research
yuki.saito@zozo.com

February 3, 2026

ABSTRACT

In image classification scenarios where both prediction and explanation efficiency are required, self-explaining models that perform both tasks in a single inference are effective. However, for users who already have prediction-only models, training a new self-explaining model from scratch imposes significant costs in terms of both labeling and computation. This study proposes a method to transfer the visual explanation capability of self-explaining models learned in a source domain to prediction-only models in a target domain based on a task arithmetic framework. Our self-explaining model comprises an architecture that extends Vision Transformer-based prediction-only models, enabling the proposed method to endow explanation capability to many trained prediction-only models without additional training. Experiments on various image classification datasets demonstrate that, except for transfers between less-related domains, the transfer of visual explanation capability from source to target domains is successful, and explanation quality in the target domain improves without substantially sacrificing classification accuracy.

1 Introduction

Visual explainability, which provides human-understandable explanations for prediction model’s outputs, is important for various applications, such as medical image diagnosis [1], autonomous driving [2], manufacturing [3], cybersecurity [4], and model debugging [5].

Although explanations provide valuable insights to users, generating them often incurs significantly higher computational costs compared to performing prediction alone. When a trained model is already available, visual explanations can be generated using post-hoc explanation methods, such as SHAP [6] and Grad-CAM [7]. However, generating an explanation for a single image with SHAP typically requires at least hundreds of model inferences, and computing Grad-CAM necessitates calculating gradients of the model’s parameters, which requires resources for backward computation. Such computational challenges can be addressed by using *self-explaining models*, which are designed to perform both prediction and explanation in a single inference [8, 9]. Although self-explaining models are very efficient in the inference phase, their training incurs high computational costs due to the need to create ground-truth explanation data for user-desired explanations [10] or the requirement for numerous model forward computations to learn these explanations [11].

The goal of this study is to efficiently equip self-explaining models with visual explainability to address such computational challenges. To this end, we focus on *task arithmetic* [12], which enables model editing using *task vectors* that

represent the model’s capabilities learned for different tasks across different domains. Interestingly, task vectors can represent *task analogies* expressed as “A is to B as C is to D,” where A and B are tasks in one domain (source domain), and C and D are tasks in another domain (target domain). If this analogy holds, the task vector for D can be inferred from those for A, B, and C, indicating that we can obtain the model parameters for task D without additional training of the model on that task.

Inspired by the idea, we propose a method to transfer the visual explainability of self-explaining models learned in a source domain to prediction-only models in a target domain through task arithmetic. Our self-explaining model is an extension of image classifiers based on vision-language models (VLMs), such as the Contrastive Language-Image Pretraining (CLIP) [13], which are designed to infer patch-level attributions from patch embeddings and the text embeddings of class labels, as well as to predict the logits of class labels similarly to prediction-only VLM-based image classifiers (Figure 1). Our model is trained on labeled image datasets with and without explanation supervision in the source domain. The difference between these two types of learned model parameters constitutes the task vector for explainability, which we refer to as the *explainability vector*. Based on the analogy for explainability: “prediction-only is to prediction-with-explanation in the source domain as prediction-only is to prediction-with-explanation in the target domain,” we provide a method to transfer explainability to a model that has been trained only for prediction in the target domain, by leveraging the explainability vector acquired in the source domain.

Our contributions can be summarized as follows:

- We propose the first task-arithmetic approach to transfer visual explainability across domains without additional training in the target domain, by defining an explainability vector as a task vector induced by explanation supervision.
- We demonstrate that explainability can be transferred to prediction-only models by evaluating 56 cross-domain dataset pairs, improving explanation quality while largely preserving classification accuracy.
- We introduce ImageNet+X, an extension of ImageNet-1k augmented with explanation supervision, and show that an explainability vector learned on ImageNet+X consistently improves explainability metrics across ten diverse target datasets.
- We show that self-explaining models enabled by our method produce competitive patch-level explanations with a single forward pass, matching the quality of expensive post-hoc explainers that require hundreds to thousands of model evaluations.

2 Related Work

Task Arithmetic Task arithmetic [12] is a weight aggregation approach in model merging. A key feature of task arithmetic is that it allows for the composition or removal of skills that models have acquired through learning, without requiring additional training. Leveraging this, studies on model editing have explored topics such as adding mathematical reasoning capabilities [14], improving fairness [15], unlearning [16], and mitigating bias [17]. However, the capability of task arithmetic for transferring visual explainability remains unexplored.

Self-Explaining Vision Models To improve the faithfulness and computational efficiency of explanations, various self-explaining models that are capable of performing both prediction and explanation have been proposed [18, 9]. As with our study, several studies have also addressed training self-explaining models to directly produce Shapley value-based explanations [11, 19]. These approaches guarantee that the explanations approximate Shapley values through the design of the objective function or network architecture, without requiring precomputed ground-truth Shapley value explanations. Similar approaches have been proposed in the research on amortized explainers [20], which learn the behavior of post-hoc explainers for a trained prediction model in advance and generate only explanations efficiently in the inference phase. Similar to ours, Covert et al. proposed a method that trains a Vision Transformer (ViT) to output patch-level attributions based on Shapley values from patch tokens [21]. While this approach can efficiently train models to produce Shapley value explanations, it is difficult to generalize it to explanations other than Shapley values due to its specialization.

Visual Explainability Transfer Some studies have proposed methods for transferring visual explainability to other domains. Transferrable Vision Explainer (TVE) [22] pretrains an encoder on a large-scale dataset like ImageNet to output meta-attribute vectors from images. In the inference phase, it uses a combination of this encoder and a pretrained classification head for the target task to output patch contributions. Although TVE is an amortized explainer and thus addresses a different problem than our method for self-explaining models, its objective of transferring pretrained explainability is consistent with the spirit of this study. Li et al. [23] demonstrated that transferring attention patterns from teacher to student models in ViT enables the student to achieve performance comparable to that of the teacher.

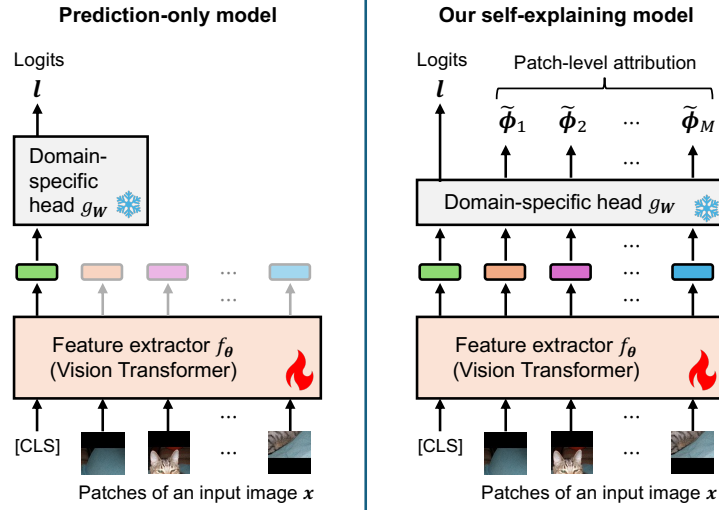


Figure 1: Model architectures of prediction-only model (left) and our self-explaining model (right). Gray boxes represent functions with fixed parameters. All the learnable parameters θ are only in the feature extractor (filled in orange).

Since attention patterns are often interpreted as explanations for model predictions, this method can be regarded as a form of explainability transfer. However, their results showed that such transfer is ineffective when the student and teacher models are trained on different domains.

3 Task Arithmetic

In this section, we introduce the task arithmetic framework [12], which serves as the foundation for our approach. Task arithmetic edits neural network models by leveraging differences in their parameter spaces. The central idea is that the effect of learning a specific capability (or task) can be represented as a vector in the parameter space, and these vectors for different tasks can be algebraically combined to transfer or compose capabilities across models. The validity of task arithmetic is supported by the observations that aggregating models by adding multiple model parameters can improve model performance [24–29].

Formally, let $\theta_{\text{base}} \in \mathbb{R}^D$ denote the parameters of a base model where D is the dimensionality of the model parameters, and let $\theta_{\text{ft}} \in \mathbb{R}^D$ denote the parameters of the same model after fine-tuning on a specific task from the base parameters θ_{base} . The difference $\tau = \theta_{\text{ft}} - \theta_{\text{base}}$ is called the *task vector* for that task, which hopefully contains the knowledge and capabilities necessary to perform the task. The addition operation of task vectors allows us to construct a model that is capable of performing multiple tasks simultaneously, similar to multi-task learning. Specifically, given multiple task vectors $\{\tau_m\}_{m=1}^M$, where m is a task index, a new model composed of capabilities from these tasks can be constructed as

$$\theta = \theta_{\text{base}} + \lambda \sum_{m=1}^M \tau_m, \quad (1)$$

where $\lambda \in \mathbb{R}$ is a scaling factor controlling the extent to which the capabilities are added (if $\lambda > 0$) or removed (if $\lambda < 0$).

For a more complicated arithmetic operation that we are interested in, analogical relationships between tasks can be considered. Suppose we have models finetuned for tasks A and B in the same domain (referred to as *source domain* for convenience), and for task C in another domain (referred to as *target domain* for convenience). Our aim is to obtain model parameters θ that achieve a new task D in target domain. If the relationship between A and B is analogous to that between C and D, we can estimate the parameters for task D using the following analogy:

$$\tau_A - \tau_B \approx \tau_C - \tau_D \quad \rightarrow \quad \tau_D \approx \tau_C - \tau_A + \tau_B. \quad (2)$$

Then, we can endow the model with the capability for task D by adding the task vector τ_D to the base parameters θ_{base} as follows:

$$\theta = \theta_{\text{base}} + \lambda \tau_D. \quad (3)$$

This property enables us to transfer learned capabilities from a source domain to a target domain, even when direct supervision in the target domain (for task \mathcal{D} in (2)) is unavailable. In the next section, we describe how we leverage task arithmetic to transfer the visual explainability of self-explaining models in the source domain to from prediction-only models in the target domains.

4 Proposed Method

4.1 Model

The proposed method requires a self-explaining image classifier model that predicts both the logits of class labels and infers patch-level attributions corresponding to the contributions of the patches for each class. As a requirement for the model to utilize task arithmetic, it is necessary that the model is represented by parameters $\theta \in \mathbb{R}^D$ even if the source and target label sets are different. In other words, the model should be capable of zero-shot classification. To satisfy the requirement, our self-explaining model is designed as shown in Figure 1, which is an extension of “prediction-only” VLM-based image classifiers [13]. More specifically, the self-explaining model consists of a feature extractor and a domain-specific head. We denote the input space as \mathcal{X} , and the number of patches in an input image as M . The feature extractor f_θ is a neural network with the Vision Transformer (ViT) architecture [30]. It takes M patches of an input image $\mathbf{x} \in \mathcal{X}$ and a special token [CLS] as input and outputs $M + 1$ K -dimensional feature vectors. The domain-specific head is a linear function $g_{\mathbf{W}} : \mathbb{R}^K \rightarrow \mathbb{R}^C$ with weights $\mathbf{W} \in \mathbb{R}^{K \times C}$ where C is the number of classes. The function $g_{\mathbf{W}}$ maps the feature vector for [CLS] to logits $\mathbf{l} = [l_1, l_2, \dots, l_C]^\top \in \mathbb{R}^C$ and that for the m th patch to unnormalized patch-level attributions $\tilde{\phi}_m = [\tilde{\phi}_{m1}, \tilde{\phi}_{m2}, \dots, \tilde{\phi}_{mC}]^\top \in \mathbb{R}^C$, respectively, where $m \in \{1, 2, \dots, M\}$ is a patch index. We denote all the patch-level attributions as $\tilde{\Phi} = [\tilde{\phi}_1, \tilde{\phi}_2, \dots, \tilde{\phi}_M] \in \mathbb{R}^{C \times M}$. \mathbf{W} is constructed by the text embeddings representing the class names generated by the text encoder of the VLM¹, i.e., $\mathbf{W}_{\cdot,c} \in \mathbb{R}^K$ is the text embedding associated with the c th class. In our model, \mathbf{W} is fixed during training; therefore, it is not included in the model parameters. The key difference from the prediction-only VLM-based image classifier, is that the domain-specific head is used for predicting not only the logits but also patch-level attributions, while the prediction-only one only predicts the logits.

Our model can reuse the pretrained parameters of the VLM-based image classifiers as the base parameters θ_{base} . Note that they do not have the capability to explain the classification results because the VLM-based image classifiers are not optimized for explanation.

4.2 Learning Classification Capability and Explainability

We acquire explainability on a source domain by finetuning our self-explaining model in a supervised manner. First, we construct a source dataset, a labeled image dataset with explanation supervision $\mathcal{D}^S = \{(\mathbf{x}^{(n)}, y^{(n)}, \phi^{(n)})\}_{n=1}^{N^S}$ where $\mathbf{x}^{(n)} \in \mathcal{X}$ is the n th input image, $y^{(n)} \in \{1, 2, \dots, C^S\}$ is the ground-truth class label of the input $\mathbf{x}^{(n)}$, and $\phi^{(n)} \in \mathbb{R}^M$ is the ground-truth patch-level attributions given $\mathbf{x}^{(n)}$ and $y^{(n)}$. We can design the ground-truth patch-level attributions flexibly along user’s purposes and applications; they are typically given by human annotators or by computing a post-hoc explanation method, such as SHAP [6, 31] and Grad-CAM [7]. Since obtaining such attributions may be highly expensive, we assume that they are only available in the source domain.

Initialized at the base parameters θ_{base} , we learn the model parameters by solving the following optimization problem:

$$\begin{aligned} \theta_{\text{ft}\star}^S &= \arg \min_{\theta} \mathcal{L}_\alpha(\theta; \mathcal{D}^S), \quad \text{where} \\ \mathcal{L}_\alpha(\theta; \mathcal{D}^S) &= \alpha \mathcal{L}_{\text{cls}}(\theta; \mathcal{D}^S) + (1 - \alpha) \mathcal{L}_{\text{exp}}(\theta; \mathcal{D}^S), \end{aligned} \quad (4)$$

where \mathcal{L}_{cls} is the cross-entropy loss between the logits and the ground-truth class label. The explanation loss \mathcal{L}_{exp} is defined as

$$\mathcal{L}_{\text{exp}}(\theta; \mathcal{D}^S) = \frac{1}{|\mathcal{D}^S|} \sum_{n=1}^{|\mathcal{D}^S|} \|\text{Norm}(\tilde{\Phi}_{y^{(n)}}^{(n)}) - \text{Norm}(\phi^{(n)})\|_2^2, \quad (5)$$

where $\tilde{\Phi}_{y^{(n)}}^{(n)}$ is the $y^{(n)}$ th column of $\tilde{\Phi}$, which is the predicted patch-level attributions for the input $\mathbf{x}^{(n)}$ when it is classified as the $y^{(n)}$ th class; $\text{Norm}(\mathbf{u})$ is a normalization function such that $\text{Norm}(\mathbf{u}) = (\mathbf{u} - \mu_{\mathbf{u}}) / \sigma_{\mathbf{u}}$ where $\mu_{\mathbf{u}}$ and $\sigma_{\mathbf{u}}$ are the mean and standard deviation of \mathbf{u} , respectively. The hyperparameter $\alpha \in [0, 1]$ balances the two losses,

¹For example, if the class name is “cat,” we use the average of text embeddings generated by the text encoder for multiple input texts, such as “a photo of cat,” “art of the cat,” and so on.

\mathcal{L}_{cls} and \mathcal{L}_{exp} . When $\alpha = 1$, the learned parameters are identical to the finetuned parameters of the prediction-only VLM-based image classifier, $\theta_{\text{ft}}^{\text{S}}$, where the subscript ‘ft’ stands for finetuned only for classification. The case of $\alpha = 0$ results in amortized explainers [21, 32] where the learned parameters have only the explanatory capability. What we want are the model parameters $\theta_{\text{ft}\star}^{\text{S}}$ learned with $0 < \alpha < 1$ that have both the classification capability (denoted by ‘ft’) and the explainability (denoted by ‘ \star ’) in the source domain.

4.3 Transferring Visual Explainability

For the target domain, we assume that the ground-truth patch-level attributions are not available. In other words, while we cannot access the model parameters $\theta_{\text{ft}\star}^{\text{T}}$ that have both the classification capability and the explainability in the target domain, the model parameters $\theta_{\text{ft}}^{\text{T}}$, which have only the classification capability, can be obtained by optimizing $\mathcal{L}_{\text{cls}}(\theta; \bar{\mathcal{D}}^{\text{T}})$, where $\bar{\mathcal{D}}^{\text{T}}$ is the labeled image dataset for the target domain without explanation supervision. Our goal is to transfer the explainability in the source domain included in $\theta_{\text{ft}\star}^{\text{S}}$ to $\theta_{\text{ft}}^{\text{T}}$ without additional training. That is, we aim at obtaining the model parameters $\tilde{\theta}_{\text{ft}\star}^{\text{T}}$, good approximation of $\theta_{\text{ft}\star}^{\text{T}}$, that have both the classification capability and the explainability for the target domain without the ground-truth patch-level attributions for the target domain.

To this end, we utilize the task arithmetic framework introduced in Section 3. Based on the task analogy (2), the task vectors obtained from the parameters trained on the source and target domains are expected to have the following relationship:

$$\tau_{\text{ft}\star}^{\text{S}} - \tau_{\text{ft}}^{\text{S}} \approx \tau_{\text{ft}\star}^{\text{T}} - \tau_{\text{ft}}^{\text{T}}, \quad (6)$$

where $\tau_{\text{ft}\star}^{\text{S}} = \theta_{\text{ft}\star}^{\text{S}} - \theta_{\text{base}}$ and $\tau_{\text{ft}\star}^{\text{T}} = \theta_{\text{ft}\star}^{\text{T}} - \theta_{\text{base}}$ are the task vectors representing both the classification capability and explainability for the source and target domains, respectively. $\tau_{\text{ft}}^{\text{S}} = \theta_{\text{ft}}^{\text{S}} - \theta_{\text{base}}$ and $\tau_{\text{ft}}^{\text{T}} = \theta_{\text{ft}}^{\text{T}} - \theta_{\text{base}}$ are the task vectors representing only the classification capability for the source and target domains, respectively. The equality in (6) holds if and only if $\tau_{\star}^{\text{S}} = \tau_{\star}^{\text{T}}$, where $\tau_{\star}^{\text{S}} = \theta_{\text{ft}\star}^{\text{S}} - \theta_{\text{ft}}^{\text{S}}$ and $\tau_{\star}^{\text{T}} = \theta_{\text{ft}\star}^{\text{T}} - \theta_{\text{ft}}^{\text{T}}$ are the task vectors representing the explainability for the source and target domains, respectively. We refer to τ_{\star}^{S} and τ_{\star}^{T} as *explainability vectors* for the source and target domains, respectively.

From (6), if $\tau_{\star}^{\text{S}} = \tau_{\star}^{\text{T}}$ holds, $\tau_{\text{ft}\star}^{\text{T}}$ can be expressed as

$$\begin{aligned} \tau_{\text{ft}\star}^{\text{T}} &= \underbrace{\theta_{\text{ft}}^{\text{T}} - \theta_{\text{base}}}_{\tau_{\text{ft}}^{\text{T}}} + \underbrace{\theta_{\text{ft}\star}^{\text{S}} - \theta_{\text{base}}}_{\tau_{\text{ft}\star}^{\text{S}}} - \underbrace{(\theta_{\text{ft}}^{\text{S}} - \theta_{\text{base}})}_{\tau_{\text{ft}}^{\text{S}}} \\ &= \underbrace{\theta_{\text{ft}}^{\text{T}} - \theta_{\text{base}}}_{\tau_{\text{ft}}^{\text{T}}} + \underbrace{\theta_{\text{ft}\star}^{\text{S}} - \theta_{\text{ft}}^{\text{S}}}_{\tau_{\star}^{\text{S}}}. \end{aligned} \quad (7)$$

Then, we can obtain the model parameters $\tilde{\theta}_{\text{ft}\star}^{\text{T}}$ by adding the task vector $\tau_{\text{ft}\star}^{\text{T}}$ to the base parameters θ_{base} . Introducing two scaling coefficients, $\lambda_1 \in \mathbb{R}$ for classification capability and $\lambda_2 \in \mathbb{R}$ for explainability, we have

$$\tilde{\theta}_{\text{ft}\star}^{\text{T}} = \theta_{\text{base}} + \lambda_1 \tau_{\text{ft}}^{\text{T}} + \lambda_2 \tau_{\star}^{\text{S}}. \quad (8)$$

Since λ_1 and λ_2 are hyperparameters that do not affect model training, they can be tuned efficiently.

5 Theoretical Interpretation

In this section, we briefly provide a theoretical interpretation of the explainability vectors τ_{\star}^{S} and τ_{\star}^{T} . A more detailed version of this section is provided in Appendix A.

τ_{\star} as Optimal Perturbation First, we show that the explainability vector τ_{\star}^{S} can be interpreted as the optimal perturbation under a local quadratic approximation of the loss function in (4) around $\theta_{\text{ft}}^{\text{S}}$. Note that the same derivation can be applied to τ_{\star}^{T} . The loss function consists of the classification loss \mathcal{L}_{cls} and the explanation loss \mathcal{L}_{exp} , each of which is approximated with Taylor expansions around $\theta_{\text{ft}}^{\text{S}}$, as follows:

$$\mathcal{L}_{\text{cls}}(\theta_{\text{ft}}^{\text{S}} + \tau; \bar{\mathcal{D}}^{\text{S}}) \approx \mathcal{L}_{\text{cls}}(\theta_{\text{ft}}^{\text{S}}; \bar{\mathcal{D}}^{\text{S}}) + \frac{1}{2} \tau^{\top} \mathbf{H}^{\text{S}} \tau, \quad (9)$$

$$\mathcal{L}_{\text{exp}}(\theta_{\text{ft}}^{\text{S}} + \tau; \mathcal{D}^{\text{S}}) \approx \mathcal{L}_{\text{exp}}(\theta_{\text{ft}}^{\text{S}}; \mathcal{D}^{\text{S}}) + (\mathbf{g}^{\text{S}})^{\top} \tau, \quad (10)$$

where $\tau \in \mathbb{R}^D$ is a small perturbation, $\mathbf{H}^{\text{S}} = \nabla^2 \mathcal{L}_{\text{cls}}(\theta_{\text{ft}}^{\text{S}}; \bar{\mathcal{D}}^{\text{S}})$ is the Hessian matrix of \mathcal{L}_{cls} at $\theta_{\text{ft}}^{\text{S}}$, and $\mathbf{g}^{\text{S}} = \nabla \mathcal{L}_{\text{exp}}(\theta_{\text{ft}}^{\text{S}}; \mathcal{D}^{\text{S}})$ is the gradient vector of \mathcal{L}_{exp} at $\theta_{\text{ft}}^{\text{S}}$.

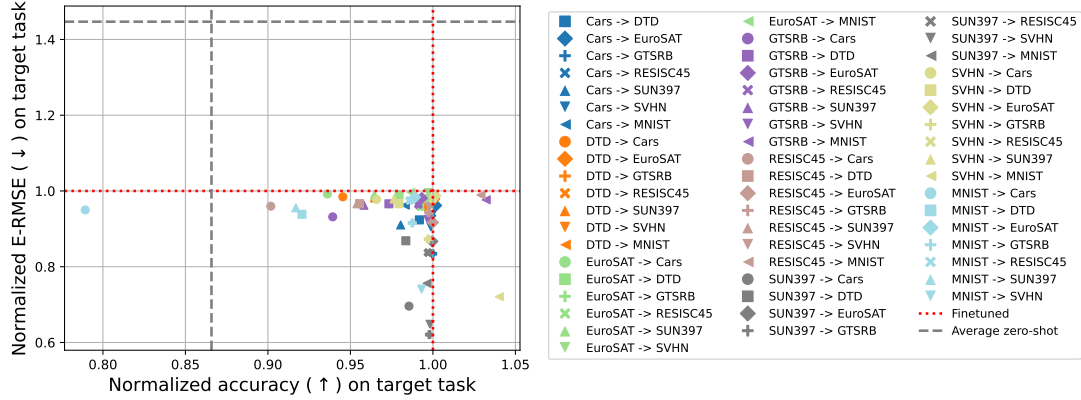


Figure 2: Normalized accuracies (larger is better) and normalized E-RMSEs (lower is better) in all the pairs of the eight benchmark datasets when fixed in $\alpha = 0.8$, $\lambda_1 = 1.0$, and $\lambda_2 = 0.7$. The color and shape of each marker indicate the source and target domains of the corresponding dataset pair, respectively.

Substituting (9) and (10) into (4), and solving τ that minimizes the approximated loss function, we obtain:

$$\tau_*^S \approx -\frac{1-\alpha}{\alpha} (\mathbf{H}^S)^{-1} \mathbf{g}^S. \quad (11)$$

The gradient vector \mathbf{g}^S represents the direction in which the explanation loss \mathcal{L}_{exp} decreases most rapidly around θ_{ft}^S . However, simply moving θ_{ft}^S in that direction could significantly degrade classification performance. The Hessian matrix \mathbf{H}^S represents the curvature of the classification loss \mathcal{L}_{cls} , and multiplying its inverse $(\mathbf{H}^S)^{-1}$ by \mathbf{g}^S has the effect of suppressing the direction in which the classification loss increases at \mathbf{g}^S . The hyperparameter α controls the magnitude of τ_*^S .

Risk of Classification Accuracy Drop In the case that explainability vectors learned in different domains are not identical, adding the source-domain explainability vector τ_*^S to the target-domain parameters θ_{ft}^T may cause a degradation in classification performance in the target domain. Based on the approximated classification loss (9), the increase in classification loss when adding the source-domain explainability vector τ_*^S to the target-domain parameters θ_{ft}^T can be quantified as

$$R(\tau_*^S; \mathbf{H}^T) = (\tau_*^S)^\top \mathbf{H}^T \tau_*^S. \quad (12)$$

By performing an eigenvalue decomposition of \mathbf{H}^T and rewriting (12) in terms of its eigenvalues and eigenvectors, we can see that if τ_*^S has a large component along eigenvectors associated with large eigenvalues of \mathbf{H}^T , then the increase in the classification loss, $R(\tau_*^S; \mathbf{H}^T)$, will be significant.

6 Experiments

We conducted experiments on various image classification datasets to evaluate the effectiveness of the proposed method in explainability transfer. Throughout experiments in this section, we used CLIP with ViT-B/32 [30] as the self-explaining model, and its base parameters θ_{base} were the pre-trained parameters learned on DataComp-1B [33, 34]. The model input is a 224×224 RGB image, each patch size of an image is 32×32 , and the number of patches in an image is $M = 49$. The hyperparameter λ_1 was set to 1.0 to focus on investigating the effect of transferring explainability via τ_*^S while preserving high classification performance on target datasets. The remaining hyperparameters, α and λ_2 , were determined within the range of $\{0.1, 0.2, \dots, 0.9\}$ and $\{0.4, 0.5, \dots, 1.2\}$, respectively, unless otherwise specified. The computing environments for the experiments are described in Appendix B. To confirm the effectiveness in larger models, we also conducted experiments using CLIP with ViT-L/14 in Appendix D.

6.1 Transferring Explainability Between Various Domain Datasets

In our first experiment, we used eight labeled image datasets: Cars [35], DTD [36], EuroSAT [37], GTSRB [38], RESISC45 [39], SUN397 [40], SVHN [41], and MNIST [42]. We extended each of these datasets to include ground-truth patch-level attributions generated using Kernel SHAP [6, 31], which explain the classification results of the CLIP

Table 1: Average performances and their standard deviations of ViT-B/32-based self-explaining models over the 10 target datasets when transferring explainability learned on ImageNet+X, compared with those of baselines. Here, the last row shows the upper/lower bound performances achieved by finetuning on the target datasets with explanation supervision (target+X). **Bold and underlined values** indicate the best among the proposed method and the baselines for each metric, while **bold values** indicate that there is no statistically significant difference from the best, as determined by a paired t -test ($p < 0.05$).

	Param.	Accuracy (\uparrow)	E-RMSE (\downarrow)	Rank Corr. (\uparrow)	IoU@1 (\uparrow)	IoU@5 (\uparrow)	IoU@10 (\uparrow)
Zero-shot	θ_{base}	0.475 ± 0.211	1.508 ± 0.069	-0.095 ± 0.059	0.012 ± 0.006	0.040 ± 0.013	0.090 ± 0.021
Finetuned on ImageNet	$\theta_{\text{ft}}^{\text{S}}$	0.379 ± 0.239	1.528 ± 0.081	-0.128 ± 0.076	0.009 ± 0.006	0.031 ± 0.016	0.074 ± 0.026
Finetuned on ImageNet+X	$\theta_{\text{ft}^*}^{\text{S}}$	0.353 ± 0.243	1.149 ± 0.092	0.197 ± 0.063	0.106 ± 0.059	0.187 ± 0.082	0.261 ± 0.079
Finetuned on target	$\theta_{\text{ft}}^{\text{T}}$	0.890 ± 0.106	1.562 ± 0.084	-0.145 ± 0.068	0.009 ± 0.005	0.033 ± 0.013	0.076 ± 0.021
Proposed	$\tilde{\theta}_{\text{ft}^*}^{\text{T}}$	0.886 ± 0.113	1.125 ± 0.116	0.20 ± 0.061	0.133 ± 0.092	0.216 ± 0.114	0.279 ± 0.093
Finetuned on target+X	$\theta_{\text{ft}^*}^{\text{T}}$	0.909 ± 0.100	1.028 ± 0.224	0.242 ± 0.104	0.248 ± 0.217	0.291 ± 0.189	0.328 ± 0.140

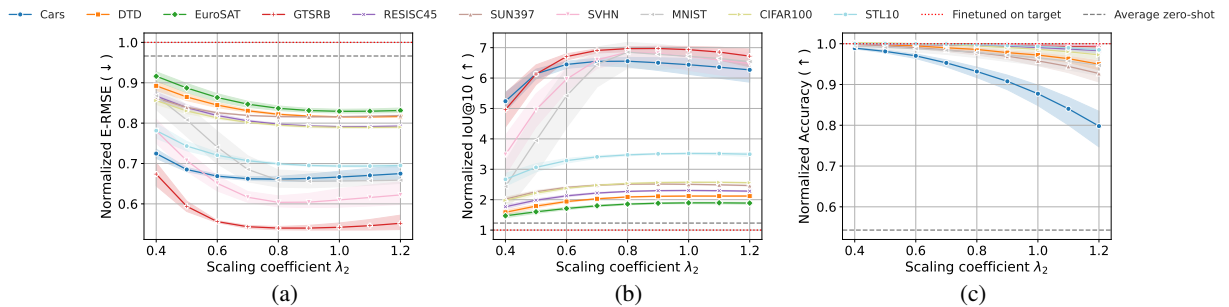


Figure 3: Normalized (a) E-RMSE, (b) IoU@10, and (c) accuracy for each target dataset over the scaling coefficient for explainability λ_2 . The shaded areas represent 95% confidence intervals of the performance for $\alpha \in \{0.1, 0.2, \dots, 0.9\}$.

image classifier finetuned on each dataset. Here, the number of perturbations for each image in Kernel SHAP is set to 500. Similar methods for generating explanation supervision have been used in previous studies [32, 43]. We created 56 dataset pairs from the eight datasets, where one dataset in each pair was used as the source dataset, and the other as the target dataset.

In the proposed method, we first learned the three types of model parameters $\theta_{\text{ft}}^{\text{S}}$, $\theta_{\text{ft}^*}^{\text{S}}$, and $\theta_{\text{ft}}^{\text{T}}$ for each dataset pair, and then obtained the model parameters $\tilde{\theta}_{\text{ft}^*}^{\text{T}}$ by applying the proposed explainability transfer (8). We evaluated the quality of $\tilde{\theta}_{\text{ft}^*}^{\text{T}}$ in terms of the classification accuracy and the explanation error using explanation root mean squared error (E-RMSE), $\sqrt{\mathcal{L}_{\text{exp}}(\theta; \mathcal{D}^{\text{T}})}$, where \mathcal{L}_{exp} is defined in (5) and \mathcal{D}^{T} is the target dataset with explanation supervision.

6.1.1 Accuracy and Explanation Error Trade-off

The first result, illustrated in Figure 2, shows the normalized accuracies and the normalized E-RMSEs for all the dataset pairs. Here, the normalized scores are obtained by dividing the corresponding scores of $\theta_{\text{ft}}^{\text{T}}$. The red dotted line indicates the performances of $\theta_{\text{ft}}^{\text{T}}$ (both the accuracy and E-RMSE are one), while the gray dashed line indicates those of the zero-shot classifier parameterized by θ_{base} . In successful cases, the E-RMSE values are decreased from one while keeping the accuracy close to one. From the figure, we found that most of the dataset pairs achieved lower E-RMSEs while maintaining at least 90% of the accuracy. In particular, the effectiveness when using SUN397 as the source dataset was notable. This is likely because SUN397 is a large-scale dataset containing diverse scene images, allowing the model to learn generalizable explanatory capabilities for various datasets. As an exception, transfer from handwritten digit recognition (MNIST) to vehicle type recognition (Cars) resulted in a significant decrease in accuracy. When transferring between two digit recognition tasks (MNIST and SVHN), accuracy was maintained or improved while E-RMSE improved substantially, suggesting that cases with significantly different domains can have adverse effects on accuracy.

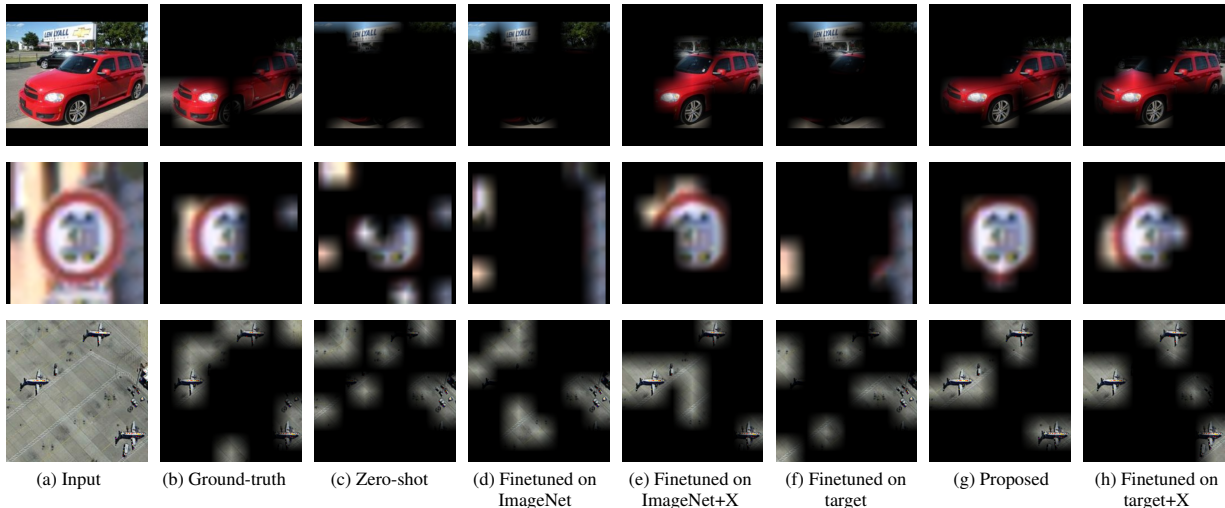


Figure 4: Visualization examples highlighting the top-10 patches in the predicted patch-level attributions. Rows show (from top to bottom) the results for Cars, GTSRB, and RESISC45 datasets.

6.2 Transferring Explainability Learned on ImageNet

In the previous section, we demonstrated that explainability acquired on a source dataset can be successfully transferred to prediction-only models on target datasets when the source dataset encompasses a diverse range of classes. This finding suggests that explainability learned on a larger and more diverse dataset, such as ImageNet, could serve as a *universal* explainability vector, transferable across a wide range of domains. To explore this potential, we investigate whether explainability learned on ImageNet can be effectively transferred to other datasets.

First, we constructed the ImageNet+X dataset, in which each sample consists of a labeled image from the original ImageNet-1k dataset and a ground-truth patch-level attribution generated in the same manner as in the previous section. As the target datasets, we used 10 image classification datasets, which include the eight datasets used in the previous section and two additional datasets: CIFAR100 [44] and STL10 [45]. As with ImageNet+X, we added the ground-truth patch-level attributions to the 10 datasets for evaluation.

In addition to classification accuracies and E-RMSEs, we also evaluated the explanation qualities using Kendall rank correlation coefficient [46, 47] (*Rank corr.* for short) and $\text{IoU}@K$ ($K \in \{1, 5, 10\}$) [48, 49]. Rank corr. measures the similarity between the rankings of predicted patch-level attributions and those of the ground-truth ones. $\text{IoU}@K$ is the intersection over union (IoU) between the predicted patch-level attributions and the ground-truth ones, which is calculated as the degree of overlap between the indices of the top- K predicted patch-level attributions and those of the top- K ground-truth ones. $\text{IoU}@K$ is useful for evaluating the correctness of highlighted patches.

6.2.1 Quantitative Results

Table 1 shows the average performances of the explainability transferred by the proposed method, in comparison to the baseline models with the parameters θ_{base} , $\theta_{\text{ft}}^{\text{S}}$, $\theta_{\text{ft}\star}^{\text{S}}$, and $\theta_{\text{ft}}^{\text{T}}$. For reference, we also show the performances of the model finetuned on the target dataset with explanation supervision, i.e., $\theta_{\text{ft}\star}^{\text{T}}$, which can be seen as the upper or lower bound of the proposed method’s performances. The table shows that compared to the baselines, the proposed method achieved the second-best accuracy while consistently achieving the best explainability performance. This represents a gap of approximately 4% compared to the upper-bound accuracy achieved by the model $\theta_{\text{ft}\star}^{\text{T}}$ and approximately 9% compared to the lower-bound E-RMSE, demonstrating that the proposed method effectively transfers explainability acquired on ImageNet+X while preserving classification capability. The method with the best accuracy was the model $\theta_{\text{ft}}^{\text{T}}$ fine-tuned on the target dataset without explanation supervision. However, this model showed the lowest or second-worst explainability performance, indicating a lack of explainability. In contrast, the second-best explainability scores were achieved by the model $\theta_{\text{ft}\star}^{\text{S}}$ fine-tuned on ImageNet+X, but this model had the lowest accuracy. The proposed method combines the highly-accurate model $\theta_{\text{ft}}^{\text{T}}$ with the explainability vector extracted from $\theta_{\text{ft}\star}^{\text{S}}$, demonstrating that the proposed method achieves the best of both worlds.

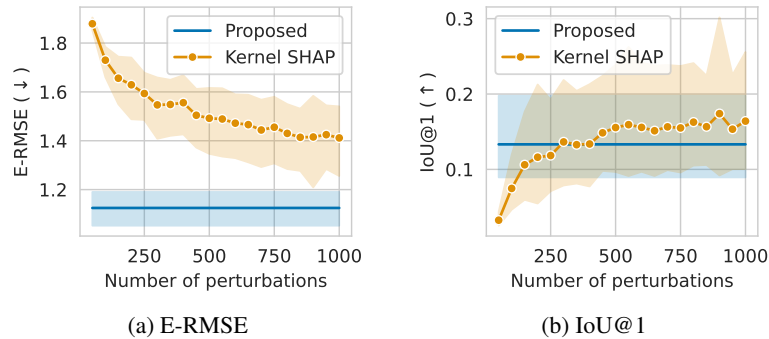


Figure 5: Explainability scores of the proposed method and Kernel SHAP averaged across the target datasets with varying number of perturbations. The shaded area represents the 95% confidence interval.

6.2.2 Impact of Scaling Coefficient

We investigated the impact of the scaling coefficient for explainability λ_2 for each target dataset. In Figure 3, we show the normalized E-RMSE, IoU@10, and accuracy for each target dataset over $\lambda_2 \in \{0.4, 0.5, \dots, 1.2\}$, where the normalized scores are obtained by dividing the corresponding scores of θ_{ft}^T . As shown in Figure 3(a) and (b), although trends vary by dataset, we found that these explainability scores improve for all target datasets. Furthermore, increasing λ_2 generally improves the explainability scores, and we observed that improvements plateau around 0.8. In Figure 3(c), classification accuracy tends to decrease as λ_2 increases, but we found that the degradation in accuracy is kept within 5% of the fine-tuned model on the target dataset when $\lambda_2 \leq 1.0$, except for Cars.

As shown in (12), a drop in classification accuracy can in principle occur depending on the relationship between the Hessian H^T and explainability vector τ_*^S , and it may arise independently of improvements in explanation quality. For Cars, increasing λ_2 led to a noticeable drop in accuracy. However, even when λ_2 is small, i.e., $\lambda_2 \leq 0.6$, the explanation performance remains very high. This suggests that, with appropriate tuning of λ_2 , it is possible to achieve a good balance between explanation quality and classification performance. In practice, this can be addressed by creating a small validation set with explanation supervision and tuning λ_2 on it.

6.2.3 Qualitative Evaluation

To evaluate the predicted patch-level attributions qualitatively, we visualized the top-10 patches in the attributions produced by the proposed method and the other methods in Figure 4. Here, this visualization aligns with the evaluation of IoU@10. As shown in the figure, the patches highlighted by the proposed method (depicted in Figure 4(g)) were more similar to the ground-truth ones (depicted in Figure 4(b)) than those highlighted by the three baseline methods that do not use any explanation supervision (depicted in Figures 4(c), (d), and (f)). Also, the model finetuned on ImageNet+X (Figure 4(e)) could generate high-quality explanations, similar to the proposed method, as was evident in the quantitative evaluation. However, due to its low classification performance, it is not practical to use this single model for both classification and prediction simultaneously.

6.2.4 Comparison with Kernel SHAP

The experiments in this section used Kernel SHAP to generate ground-truth patch-level attributions. Kernel SHAP requires classification results obtained with model inferences for hundreds to thousands of input perturbations, making it computationally expensive. In contrast, our self-explaining model predicts these attributions in a single inference. To evaluate the computational efficiency advantage of our approach, we investigated how many perturbations Kernel SHAP requires to match the explanation quality of the proposed method, $\tilde{\theta}_{ft*}^T$ (computational complexity details are in Appendix E).

Figure 5 presents average scores of E-RMSE and IoU@1 versus the number of Kernel SHAP perturbations. The results of all the scores are shown in Figure 8 in Appendix F. For all the scores except IoU@1, the proposed method substantially outperforms Kernel SHAP, even with 1,000 perturbations, demonstrating superior efficiency in generating both accurate attribution values and their rankings. For IoU@1, the proposed method achieves performance equivalent to Kernel SHAP with 300 perturbations, showing particular effectiveness for identifying the most important patch location.

7 Conclusion

We proposed a method for transferring the visual explainability of self-explaining models into prediction-only models through task arithmetic without additional training. Visual explainability is represented as an explainability vector in the model parameter space, and the proposed method can transfer this capability to a wide range of prediction-only models, thereby converting them into self-explainable models. Among the extensive experiments, the most notable finding is that an explainability vector acquired from a large-scale dataset, such as ImageNet, can effectively transfer explainability to prediction-only models trained on diverse domain-specific datasets, achieving explanation performance exceeding 90% of that of self-explaining models trained with explanation supervision. Based on this finding, we will explore the possibility of constructing a universal explainability vector using larger-scale datasets that can be applied to various downstream tasks.

References

- [1] Sajid Nazir, Diane M Dickson, and Muhammad Usman Akram. Survey of explainable artificial intelligence techniques for biomedical imaging with deep neural networks. *Computers in Biology and Medicine*, 156:106668, 2023.
- [2] Shahin Atakishiyev, Mohammad Salameh, Hengshuai Yao, and Randy Goebel. Explainable artificial intelligence for autonomous driving: A comprehensive overview and field guide for future research directions. *IEEE Access*, 2024.
- [3] Zoe Alexander, Duen Horng Chau, and Christopher Saldaña. An interrogative survey of explainable ai in manufacturing. *IEEE Transactions on Industrial Informatics*, 2024.
- [4] Nicola Capuano, Giuseppe Fenza, Vincenzo Loia, and Claudio Stanzione. Explainable artificial intelligence in cybersecurity: A survey. *IEEE Access*, 10:93575–93600, 2022.
- [5] Andrea Apicella, Luca Di Lorenzo, Francesco Isgrò, Andrea Pollastro, and Roberto Prevete. Strategies to exploit xai to improve classification systems. In *World Conference on Explainable Artificial Intelligence*, pages 147–159. Springer, 2023.
- [6] Scott M Lundberg and Su-In Lee. A Unified Approach to Interpreting Model Predictions. *Advances in Neural Information Processing Systems*, pages 4765–4774, 2017.
- [7] Ramprasaath R Selvaraju, Michael Cogswell, Abhishek Das, Ramakrishna Vedantam, Devi Parikh, and Dhruv Batra. Grad-CAM: Visual Explanations from Deep Networks via Gradient-Based Localization. *International Journal of Computer Vision*, 128(2):336–359, 2020.
- [8] David Alvarez Melis and Tommi Jaakkola. Towards robust interpretability with self-explaining neural networks. *Advances in Neural Information Processing Systems*, 31, 2018.
- [9] Yang Ji, Ying Sun, Yuting Zhang, Zhigaoyuan Wang, Yuanxin Zhuang, Zheng Gong, Dazhong Shen, Chuan Qin, Hengshu Zhu, and Hui Xiong. A comprehensive survey on self-interpretable neural networks. *arXiv preprint arXiv:2501.15638*, 2025.
- [10] Andrew Slavin Ross, Michael C Hughes, and Finale Doshi-Velez. Right for the right reasons: Training differentiable models by constraining their explanations. In *Proceedings of the Twenty-Sixth International Joint Conference on Artificial Intelligence*, pages 2662–2670. International Joint Conferences on Artificial Intelligence Organization, 2017.
- [11] Rui Wang, Xiaoqian Wang, and David Inouye. Shapley explanation networks. In *International Conference on Learning Representations*, 2021.
- [12] Gabriel Ilharco, Marco Tulio Ribeiro, Mitchell Wortsman, Suchin Gururangan, Ludwig Schmidt, Hannaneh Hajishirzi, and Ali Farhadi. Editing models with task arithmetic. *arXiv preprint arXiv:2212.04089*, 2023.
- [13] Alec Radford, Jong Wook Kim, Chris Hallacy, Aditya Ramesh, Gabriel Goh, Sandhini Agarwal, Girish Sastry, Amanda Askell, Pamela Mishkin, Jack Clark, et al. Learning transferable visual models from natural language supervision. In *International Conference on Machine Learning (ICML)*, pages 8748–8763, 2021.
- [14] Shiqi Chen, Jinghan Zhang, Tongyao Zhu, Wei Liu, Siyang Gao, Miao Xiong, Manling Li, and Junxian He. Bring reason to vision: Understanding perception and reasoning through model merging. *arXiv preprint arXiv:2505.05464*, 2025.
- [15] Laura Gomezjurado Gonzalez, Hiroki Naganuma, Kotaro Yoshida, Takafumi Horie, Yuji Naraki, and Ryotaro Shimizu. On fairness of task arithmetic: The role of task vectors. In *NeurIPS 2025 Workshop: Reliable ML from Unreliable Data*, 2025.

- [16] Shiwen Ni, Dingwei Chen, Chengming Li, Xiping Hu, Ruifeng Xu, and Min Yang. Forgetting before learning: Utilizing parametric arithmetic for knowledge updating in large language models. In *Proceedings of the 62nd Annual Meeting of the Association for Computational Linguistics (Volume 1: Long Papers)*, pages 5716–5731, 2024.
- [17] Daiki Shirafuji, Makoto Takenaka, and Shinya Taguchi. Bias vector: Mitigating biases in language models with task arithmetic approach. In *Proceedings of the 31st International Conference on Computational Linguistics*, pages 2799–2813, 2025.
- [18] Rami Ibrahim and M Omair Shafiq. Explainable convolutional neural networks: a taxonomy, review, and future directions. *ACM Computing Surveys*, 55(10):1–37, 2023.
- [19] Amr Alkhatib, Roman Bresson, Henrik Boström, and Michalis Vazirgiannis. Prediction via shapley value regression. *arXiv preprint arXiv:2505.04775*, 2025.
- [20] Yu-Neng Chuang, Guanchu Wang, Fan Yang, Zirui Liu, Xuanting Cai, Mengnan Du, and Xia Hu. Efficient xai techniques: A taxonomic survey. *arXiv preprint arXiv:2302.03225*, 2023.
- [21] Ian Connick Covert, Chanwoo Kim, and Su-In Lee. Learning to estimate shapley values with vision transformers. In *The Eleventh International Conference on Learning Representations*, 2023.
- [22] Guanchu Wang, Yu-Neng Chuang, Fan Yang, Mengnan Du, Chia-Yuan Chang, Shaochen Zhong, Zirui Liu, Zhaozhuo Xu, Kaixiong Zhou, Xuanting Cai, et al. Tve: Learning meta-attribution for transferable vision explainer. In *International Conference on Machine Learning*, pages 50248–50267. PMLR, 2024.
- [23] Alex Li, Yuandong Tian, Beidi Chen, Deepak Pathak, and Xinlei Chen. On the surprising effectiveness of attention transfer for vision transformers. *Advances in Neural Information Processing Systems*, 37:113963–113990, 2024.
- [24] P Izmailov, AG Wilson, D Podoprikin, D Vetrov, and T Garipov. Averaging weights leads to wider optima and better generalization. In *34th Conference on Uncertainty in Artificial Intelligence 2018, UAI 2018*, pages 876–885, 2018.
- [25] Arthur Jacot, Franck Gabriel, and Clément Hongler. Neural tangent kernel: Convergence and generalization in neural networks. *Advances in neural information processing systems*, 31, 2018.
- [26] Mitchell Wortsman, Gabriel Ilharco, Samir Ya Gadre, Rebecca Roelofs, Raphael Gontijo-Lopes, Ari S Morcos, Hongseok Namkoong, Ali Farhadi, Yair Carmon, Simon Kornblith, et al. Model soups: averaging weights of multiple fine-tuned models improves accuracy without increasing inference time. In *International conference on machine learning*, pages 23965–23998. PMLR, 2022.
- [27] Mitchell Wortsman, Gabriel Ilharco, Jong Wook Kim, Mike Li, Simon Kornblith, Rebecca Roelofs, Raphael Gontijo Lopes, Hannaneh Hajishirzi, Ali Farhadi, Hongseok Namkoong, et al. Robust fine-tuning of zero-shot models. In *Proceedings of the IEEE/CVF conference on computer vision and pattern recognition*, pages 7959–7971, 2022.
- [28] Kotaro Yoshida, Yuji Naraki, Takafumi Horie, Ryosuke Yamaki, Ryotaro Shimizu, Yuki Saito, Julian McAuley, and Hiroki Naganuma. Mastering task arithmetic: τ_{jp} as a key indicator for weight disentanglement. In *The Thirteenth International Conference on Learning Representations*, 2025.
- [29] Kotaro Yoshida, Yuji Naraki, Takafumi Horie, Ryotaro Shimizu, and Hiroki Naganuma. Distac: Conditioning task vectors via distillation for robust model merging. *arXiv preprint arXiv:2508.01148*, 2025.
- [30] Alexey Dosovitskiy, Lucas Beyer, Alexander Kolesnikov, Dirk Weissenborn, Xiaohua Zhai, Thomas Unterthiner, Mostafa Dehghani, Matthias Minderer, Georg Heigold, Sylvain Gelly, Jakob Uszkoreit, and Neil Houlsby. An image is worth 16x16 words: Transformers for image recognition at scale. In *International Conference on Learning Representations*, 2021. URL <https://openreview.net/forum?id=YicbFdNTTy>.
- [31] shap (Github). shap: A game theoretic approach to explain the output of any machine learning model, 2024. URL <https://github.com/shap/shap>. Accessed: 2024-2-2.
- [32] Chenghao Yang, Fan Yin, He He, Kai-Wei Chang, Xiaofei Ma, and Bing Xiang. Efficient shapley values estimation by amortization for text classification. In *Proceedings of the 61st Annual Meeting of the Association for Computational Linguistics (Volume 1: Long Papers)*, pages 8666–8680, 2023.
- [33] Samir Yitzhak Gadre, Gabriel Ilharco, Alex Fang, Jonathan Hayase, Georgios Smyrnis, Thao Nguyen, Ryan Marten, Mitchell Wortsman, Dhruva Ghosh, Jieyu Zhang, Eyal Orgad, Rahim Entezari, Giannis Daras, Sarah Pratt, Vivek Ramanujan, Yonatan Bitton, Kalyani Marathe, Stephen Mussmann, Richard Vencu, Mehdi Cherti, Ranjay Krishna, Pang Wei Koh, Olga Saukh, Alexander Ratner, Shuran Song, Hannaneh Hajishirzi, Ali Farhadi, Romain Beaumont, Sewoong Oh, Alex Dimakis, Jenia Jitsev, Yair Carmon, Vaishaal Shankar, and Ludwig Schmidt. Datacomp: In search of the next generation of multimodal datasets. *arXiv preprint arXiv:2304.14108*, 2023.

- [34] Gabriel Ilharco, Mitchell Wortsman, Ross Wightman, Cade Gordon, Nicholas Carlini, Rohan Taori, Achal Dave, Vaishal Shankar, Hongseok Namkoong, John Miller, Hannaneh Hajishirzi, Ali Farhadi, and Ludwig Schmidt. Openclip, July 2021. URL <https://doi.org/10.5281/zenodo.5143773>.
- [35] Jonathan Krause, Michael Stark, Jia Deng, and Li Fei-Fei. 3d object representations for fine-grained categorization. In *Proceedings of the IEEE international conference on computer vision workshops*, pages 554–561, 2013.
- [36] Mircea Cimpoi, Subhansu Maji, Iasonas Kokkinos, Sammy Mohamed, and Andrea Vedaldi. Describing textures in the wild. In *Proceedings of the IEEE conference on computer vision and pattern recognition*, pages 3606–3613, 2014.
- [37] Patrick Helber, Benjamin Bischke, Andreas Dengel, and Damian Borth. Eurosat: A novel dataset and deep learning benchmark for land use and land cover classification. *IEEE Journal of Selected Topics in Applied Earth Observations and Remote Sensing*, 12(7):2217–2226, 2019.
- [38] Johannes Stallkamp, Marc Schlipsing, Jan Salmen, and Christian Igel. The german traffic sign recognition benchmark: a multi-class classification competition. In *The 2011 international joint conference on neural networks*, pages 1453–1460. IEEE, 2011.
- [39] Gong Cheng, Junwei Han, and Xiaoqiang Lu. Remote sensing image scene classification: Benchmark and state of the art. *Proceedings of the IEEE*, 105(10):1865–1883, 2017.
- [40] Jianxiong Xiao, Krista A Ehinger, James Hays, Antonio Torralba, and Aude Oliva. Sun database: Exploring a large collection of scene categories. *International Journal of Computer Vision*, 119:3–22, 2016.
- [41] Yuval Netzer, Tao Wang, Adam Coates, Alessandro Bissacco, Baolin Wu, Andrew Y Ng, et al. Reading digits in natural images with unsupervised feature learning. In *NIPS workshop on deep learning and unsupervised feature learning*, volume 2011, page 4. Granada, 2011.
- [42] Yann LeCun. The mnist database of handwritten digits. <http://yann.lecun.com/exdb/mnist/>, 1998.
- [43] Lucas Monteiro Paes, Dennis Wei, and Flavio Calmon. Selective explanations. *Advances in Neural Information Processing Systems*, 37:55562–55590, 2024.
- [44] Alex Krizhevsky. Learning multiple layers of features from tiny images, 2009. URL <https://api.semanticscholar.org/CorpusID:18268744>.
- [45] Adam Coates, Andrew Ng, and Honglak Lee. An analysis of single-layer networks in unsupervised feature learning. In *Proceedings of the fourteenth international conference on artificial intelligence and statistics*, pages 215–223. JMLR Workshop and Conference Proceedings, 2011.
- [46] Maurice Kendall and Jean D Gibbons. Rank correlation methods. charles griffin book series. *London, Oxford University Press*, 10:0195208374, 1990.
- [47] Weina Jin, Xiaoxiao Li, Mostafa Fatehi, and Ghassan Hamarneh. Guidelines and evaluation of clinical explainable AI in medical image analysis. *Medical Image Analysis*, 84(102684):102684, February 2023. ISSN 1361-8415,1361-8423. doi:10.1016/j.media.2022.102684. URL <http://dx.doi.org/10.1016/j.media.2022.102684>.
- [48] Yifei Zhang, James Song, Siyi Gu, Tianxu Jiang, Bo Pan, Guangji Bai, and Liang Zhao. Saliency-bench: A comprehensive benchmark for evaluating visual explanations, 2025. URL <https://arxiv.org/abs/2310.08537>.
- [49] Kanglong Fan, Chen Ma, Yifan Peng, Yuming Fang, and Kede Ma. Decision rules are in the pixels: Towards pixel-level evaluation of saliency-based XAI models, 2024. URL <https://openreview.net/forum?id=mKGXdsq7fD>.
- [50] Jacob Goldenblat and contributors. Pytorch library for cam methods. <https://github.com/jacobgil/pytorch-grad-cam>, 2021.

A Theoretical Interpretation

In this section, we provide a theoretical interpretation of the explainability vectors τ_\star^S and τ_\star^T .

τ_\star as Optimal Perturbation First, we show that the explainability vector τ_\star^S can be interpreted as the optimal perturbation under a local quadratic approximation around θ_{fit}^S of the loss function in (4). Note that the same derivation can be applied to τ_\star^T . The loss function in (4) consists of the classification loss \mathcal{L}_{cls} and the explanation loss \mathcal{L}_{exp} .

We perform a local expansion around $\theta_{\text{ft}}^{\text{S}}$ for \mathcal{L}_{cls} . Let $\theta = \theta_{\text{ft}}^{\text{S}} + \tau$ where $\tau \in \mathbb{R}^D$ is a small perturbation. Since $\theta_{\text{ft}}^{\text{S}}$ approximately satisfies $\nabla \mathcal{L}_{\text{cls}}(\theta_{\text{ft}}^{\text{S}}; \bar{\mathcal{D}}^{\text{S}}) = \mathbf{0}$, a second-order Taylor expansion yields

$$\mathcal{L}_{\text{cls}}(\theta_{\text{ft}}^{\text{S}} + \tau; \bar{\mathcal{D}}^{\text{S}}) \approx \mathcal{L}_{\text{cls}}(\theta_{\text{ft}}^{\text{S}}; \bar{\mathcal{D}}^{\text{S}}) + \frac{1}{2} \tau^{\top} \mathbf{H}^{\text{S}} \tau, \quad (13)$$

where $\mathbf{H}^{\text{S}} = \nabla^2 \mathcal{L}_{\text{cls}}(\theta_{\text{ft}}^{\text{S}}; \bar{\mathcal{D}}^{\text{S}})$ is the Hessian matrix of \mathcal{L}_{cls} at $\theta_{\text{ft}}^{\text{S}}$. Similarly, we perform a first-order Taylor expansion of \mathcal{L}_{exp} around $\theta_{\text{ft}}^{\text{S}}$ as follows:

$$\mathcal{L}_{\text{exp}}(\theta_{\text{ft}}^{\text{S}} + \tau; \mathcal{D}^{\text{S}}) \approx \mathcal{L}_{\text{exp}}(\theta_{\text{ft}}^{\text{S}}; \mathcal{D}^{\text{S}}) + (\mathbf{g}^{\text{S}})^{\top} \tau, \quad (14)$$

where $\mathbf{g}^{\text{S}} = \nabla \mathcal{L}_{\text{exp}}(\theta_{\text{ft}}^{\text{S}}; \mathcal{D}^{\text{S}})$ is the gradient vector of \mathcal{L}_{exp} at $\theta_{\text{ft}}^{\text{S}}$. Substituting (13) and (14) into (4), and solving τ that minimizes the approximated loss function, we obtain:

$$\tau_{\star}^{\text{S}} \approx -\frac{1-\alpha}{\alpha} (\mathbf{H}^{\text{S}})^{-1} \mathbf{g}^{\text{S}}. \quad (15)$$

The gradient vector \mathbf{g}^{S} represents the direction in which the explanation loss \mathcal{L}_{exp} decreases most rapidly around $\theta_{\text{ft}}^{\text{S}}$. However, simply moving $\theta_{\text{ft}}^{\text{S}}$ in that direction could significantly degrade classification performance. The Hessian matrix \mathbf{H}^{S} represents the curvature of the classification loss \mathcal{L}_{cls} , and multiplying its inverse $(\mathbf{H}^{\text{S}})^{-1}$ by \mathbf{g}^{S} has the effect of suppressing the direction in which the classification loss increases at \mathbf{g}^{S} . The hyperparameter α controls the magnitude of τ_{\star}^{S} : as α approaches one, the magnitude of τ_{\star}^{S} decreases, and from (7), classification accuracy is prioritized.

Risk of Classification Accuracy Drop In the case that explainability vectors learned in different domains are not identical, adding the source-domain explainability vector τ_{\star}^{S} to the target-domain parameters $\theta_{\text{ft}}^{\text{T}}$ may cause a degradation in classification performance in the target domain. Formally, based on the approximated classification loss (13), the increase in classification loss when adding the source-domain explainability vector τ_{\star}^{S} to the target-domain parameters $\theta_{\text{ft}}^{\text{T}}$ can be quantified as

$$R(\tau_{\star}^{\text{S}}; \mathbf{H}^{\text{T}}) = (\tau_{\star}^{\text{S}})^{\top} \mathbf{H}^{\text{T}} \tau_{\star}^{\text{S}}. \quad (16)$$

To understand the property of this function, we perform eigenvalue decomposition of \mathbf{H}^{T} as

$$\mathbf{H}^{\text{T}} = \mathbf{U} \mathbf{\Lambda} \mathbf{U}^{\top}, \quad \mathbf{\Lambda} = \text{diag}(\lambda_1, \lambda_2, \dots, \lambda_P), \quad (17)$$

$$(\lambda_1 \geq \lambda_2 \geq \dots \geq \lambda_P \geq 0).$$

Here, $\mathbf{U} = [\mathbf{u}_1, \mathbf{u}_2, \dots, \mathbf{u}_P]$ is the matrix of orthonormal eigenvectors of \mathbf{H}^{T} , and $\mathbf{\Lambda}$ is the diagonal matrix of eigenvalues of \mathbf{H}^{T} . Expanding τ_{\star}^{S} in the eigenvector basis of \mathbf{H}^{T} yields

$$\tau_{\star}^{\text{S}} = \sum_{i=1}^P a_i \mathbf{u}_i, \quad a_i = (\tau_{\star}^{\text{S}})^{\top} \mathbf{u}_i. \quad (18)$$

Then (16) can be rewritten as

$$R(\tau_{\star}^{\text{S}}; \mathbf{H}^{\text{T}}) = \sum_{i=1}^P \lambda_i a_i^2. \quad (19)$$

This expression indicates that if τ_{\star}^{S} has a large component in the direction of the eigenvectors associated with large eigenvalues of \mathbf{H}^{T} , the increase in classification loss $R(\tau_{\star}^{\text{S}}; \mathbf{H}^{\text{T}})$ will be significant.

If a precomputed Hessian matrix \mathbf{H}^{T} is available, we can select the explainability vector τ_{\star}^{S} that minimizes $R(\tau_{\star}^{\text{S}}; \mathbf{H}^{\text{T}})$ among candidates learned in different source domains, without accessing any data from the target domain. However, storing the precomputed \mathbf{H}^{T} , a dense matrix whose size scales quadratically with the number of model parameters, is infeasible; therefore, in practice it is reasonable to approximate it with a diagonal matrix.

Evaluating $\tau_{\star}^{\text{S}} = \tau_{\star}^{\text{T}}$ To predict the success of explainability transfer, it is important to accurately assess whether the sufficient condition for (8), $\tau_{\star}^{\text{S}} = \tau_{\star}^{\text{T}}$, holds. The extent to which $\tau_{\star}^{\text{S}} = \tau_{\star}^{\text{T}}$ holds is appropriate to be quantified by the cosine similarity of τ_{\star}^{S} and τ_{\star}^{T} because the norm of the explainability vectors can be controlled with the hyperparameters α and λ_2 . However, since τ_{\star}^{T} and \mathbf{g}^{T} are unknown due to the lack of explanation supervision in the target domain, we need to indirectly evaluate them using observable alternative variables. According to (15), the explainability vector τ_{\star}^{T} depends on the Hessian matrix \mathbf{H}^{T} , which represents the curvature of the classification loss. If the Hessian matrices \mathbf{H}^{S} and \mathbf{H}^{T} are similar, then the explainability vectors τ_{\star}^{S} and τ_{\star}^{T} may also be similar. Therefore, as an alternative, we propose to use the cosine similarity of $\tau_{\text{ft}}^{\text{S}}$ and $\tau_{\text{ft}}^{\text{T}}$. The validity of the approximation is empirically supported by the observation that the similarity of τ_{\star}^{S} and τ_{\star}^{T} is significantly correlated with that of $\tau_{\text{ft}}^{\text{S}}$ and $\tau_{\text{ft}}^{\text{T}}$ (Pearson's $r = 0.73$, $p < 0.01$), as shown in Appendix C.

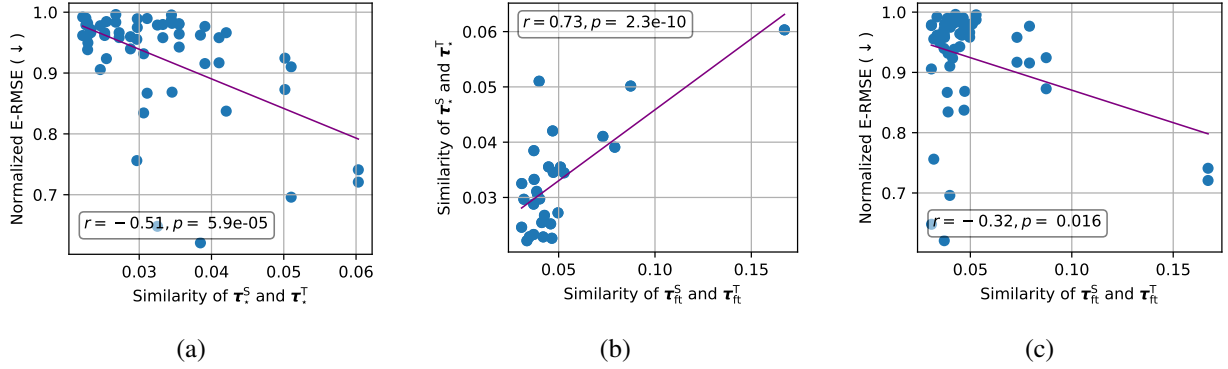


Figure 6: Relationships between two values for each dataset pair indicated in a blue point: (a) the similarity of τ_*^S and τ_*^T and E-RMSE, (b) the similarity of τ_*^S and τ_*^T and that of τ_{ft}^S and τ_{ft}^T , and (c) the similarity of τ_{ft}^S and τ_{ft}^T and E-RMSE. The purple solid line shows the least-squares regression fitted to the blue points, and the Pearson’s correlation coefficient r and its p -value are reported in the box of each panel.

B Computing Environment for Experiments

The experiments were conducted in parallel on Rocky Linux machines with two Intel Xeon Platinum 8558 2.1GHz (48 cores) CPUs, 2,048 GB of RAM, and eight NVIDIA H200 SXM GPUs with 141GB of memory. The code was implemented in Python 3.9.21 using PyTorch 2.6.

C Impact of Similarity of Explainability Vectors

The task analogy (6) strictly holds if and only if $\tau_*^S = \tau_*^T$. In practice, the difference of the norms between τ_*^S and τ_*^T does not affect the performance because we take τ_*^S into account with the scalar multiplication by λ_2 as in (8). Thus, we evaluated the extent to which this condition holds using the cosine similarity of the explainability vectors τ_*^S and τ_*^T , which focuses on evaluating the alignment of the vectors’ directions rather than their scaling. Assessing the relationship between the performance of explainability transfer and the similarity of τ_*^S and τ_*^T is an important task to bridge the theory and the experimental result. Figure 6(a) shows the relationship between the similarity of τ_*^S and τ_*^T and the E-RMSE for each dataset pair, and we observed a statistically significant negative correlation between the similarity of the explainability vectors and the E-RMSE (Pearson’s $r = -0.51$, $p < 0.01$). This result indicates that a higher similarity between explainability vectors could lead to a lower E-RMSE, indicating better explainability transfer.

Since the similarity of τ_*^S and τ_*^T cannot be directly evaluated due to the unknown τ_*^T , we approximated it using the similarity of τ_{ft}^S and τ_{ft}^T , which can be computed without explanation supervision. Figure 6(b) shows the relationship between the two similarities, and we found a statistically significant and strongly positive correlation between them (Pearson’s $r = 0.73$, $p < 0.01$).

Building on these results, we investigated whether the similarity of τ_{ft}^S and τ_{ft}^T could serve as a predictor for the success of explainability transfer. Figure 6(c) shows the relationship between the similarity of τ_{ft}^S and τ_{ft}^T and the E-RMSE for each dataset pair, and we found a statistically significant negative correlation between them (Pearson’s $r = -0.32$, $p < 0.01$). Although a significant correlation was observed, it is important to note that the correlation was weaker than that between the similarity of τ_*^S and τ_*^T and the E-RMSE. This suggests that we should utilize the similarity of τ_{ft}^S and τ_{ft}^T carefully for predicting the success of explainability transfer.

D Experiments with ViT-L/14

To validate the effectiveness of the proposed method with a larger vision transformer, we conducted experiments using ViT-L/14 as the backbone of the self-explaining image classifier.

D.1 Setup

The model input is a 224×224 image, which is split into 16×16 patches of size 14×14 . Therefore, the number of patches M is 256.

Table 2: Average performances and their standard deviations of ViT-L/14-based self-explaining models over the 10 target datasets when transferring explainability learned on ImageNet+X, compared with those of baselines. Here, the last row shows the upper/lower bound performances achieved by finetuning on the target datasets with explanation supervision (target+X). **Bold and underlined values** indicate the best among the proposed method and the baselines for each metric, while **bold values** indicate that there is no statistically significant difference from the best, as determined by a paired t -test ($p < 0.05$).

	Param.	Accuracy (\uparrow)	E-RMSE (\downarrow)	Rank Corr. (\uparrow)	IoU@1 (\uparrow)	IoU@5 (\uparrow)	IoU@10 (\uparrow)
Zero-shot	θ_{base}	0.630 ± 0.151	1.470 ± 0.043	-0.050 ± 0.028	0.003 ± 0.002	0.007 ± 0.004	0.014 ± 0.006
Finetuned on ImageNet	$\theta_{\text{ft}}^{\text{S}}$	0.542 ± 0.190	1.486 ± 0.052	-0.072 ± 0.042	0.002 ± 0.001	0.005 ± 0.003	0.011 ± 0.005
Finetuned on ImageNet+X	$\theta_{\text{ft}^*}^{\text{S}}$	0.501 ± 0.197	1.256 ± 0.078	0.121 ± 0.059	0.011 ± 0.007	0.030 ± 0.015	0.053 ± 0.024
Finetuned on target	$\theta_{\text{ft}}^{\text{T}}$	0.940 ± 0.065	1.493 ± 0.058	-0.069 ± 0.038	0.001 ± 0.001	0.005 ± 0.003	0.010 ± 0.005
Proposed	$\hat{\theta}_{\text{ft}^*}^{\text{T}}$	0.928 ± 0.072	1.253 ± 0.106	0.117 ± 0.072	0.015 ± 0.017	0.042 ± 0.050	0.067 ± 0.063
Finetuned on target+X	$\theta_{\text{ft}^*}^{\text{T}}$	0.943 ± 0.069	1.236 ± 0.086	0.123 ± 0.049	0.016 ± 0.012	0.045 ± 0.032	0.075 ± 0.048

The ground-truth patch-level attributions for ImageNet and the 10 target datasets, Cars [35], DTD [36], EuroSAT [37], GTSRB [38], RESISC45 [39], SUN397 [40], SVHN [41], MNIST [42], CIFAR100 [44], and STL10 [45], are obtained by applying Grad-CAM [7], implemented by `pytorch-grad-cam` [50], to the finetuned ViT-L/14-based image classifiers for each dataset. Specifically, we apply Grad-CAM to the layer normalization of the final residual block in the Vision Transformer encoder. The obtained patch-level attributions are pixel-wise values, therefore, we aggregate them into patch-level attribution values by averaging the pixel-wise attribution values within each patch.

D.2 Quantitative Results

Table 2 shows the average performances of the explainability transferred by the proposed method with $\alpha = 0.8$ in (5) and $\lambda_1 = 1.0$, $\lambda_2 = 0.7$ in (8), in comparison to the baseline models with the parameters θ_{base} , $\theta_{\text{ft}}^{\text{S}}$, $\theta_{\text{ft}^*}^{\text{S}}$, and $\theta_{\text{ft}}^{\text{T}}$. For reference, we also show the performances of the model finetuned on the target dataset with explanation supervision, i.e., $\theta_{\text{ft}^*}^{\text{T}}$, which can be seen as the upper or lower bound of the proposed method’s performances. The table shows that compared to the baselines, the proposed method achieved the second-best accuracy while achieving the best or second-best explainability performances. This represents a gap of approximately 2% compared to the upper-bound accuracy achieved by the model $\theta_{\text{ft}^*}^{\text{T}}$ and approximately 2% compared to the lower-bound E-RMSE, demonstrating that the proposed method effectively transfers explainability acquired on ImageNet+X while preserving classification capability. The method with the best accuracy was the model $\theta_{\text{ft}}^{\text{T}}$ fine-tuned on the target dataset without explanation supervision. However, this model showed the worst or second-worst explainability performances, indicating a lack of explainability. In contrast, the best Rank Corr. was achieved by the model $\theta_{\text{ft}^*}^{\text{S}}$ fine-tuned on ImageNet+X, but this model had the lowest accuracy. The proposed method combines the highly-accurate model $\theta_{\text{ft}}^{\text{T}}$ with the explainability vector extracted from $\theta_{\text{ft}^*}^{\text{S}}$, demonstrating that the proposed method achieves the best of both worlds.

Overall, the classification accuracy was improved compared to the ViT-B/32-based models shown in Table 1 because of the larger model capacity of ViT-L/14. On the other hand, the explainability performance scores were lower than those of the ViT-B/32-based models. This is because the quality of ground-truth patch-level attributions obtained from Grad-CAM is slightly lower, and the higher patch resolution than that of ViT-B/32 increases the difficulty of attribution prediction.

D.3 Qualitative Evaluation

To evaluate the predicted patch-level attributions qualitatively, we visualized the top-20 patches in the attributions produced by the proposed method and the other methods in Figure 7. The visualization results were similar to those of ViT-B/32 shown in Figure 4. In particular, the patches highlighted by the proposed method (depicted in Figure 7(g)) were more similar to the ground-truth ones (depicted in Figure 7(b)) than those highlighted by the three baseline methods that do not use any explanation supervision (depicted in Figures 7(c), (d), and (f)). Also, the model finetuned on ImageNet+X (Figure 7(e)) could generate high-quality explanations, similar to the proposed method, as was evident in the quantitative evaluation. However, due to its low classification performance shown in Table 2, it is not practical to use this single model for both classification and prediction simultaneously. Although the model finetuned on the target dataset with explanation supervision could produce the explanations most similar to the ground-truth ones overall were

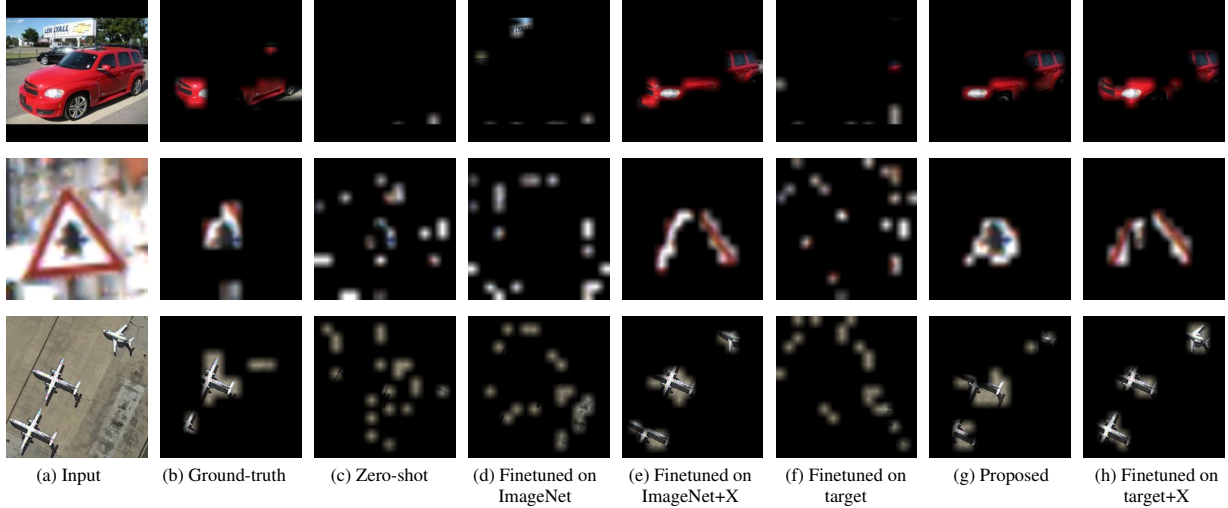


Figure 7: Visualization examples highlighting the top-20 patches in the predicted patch-level attributions produced using ViT-L/14 self-explaining image classifiers. Rows show (from top to bottom) the results for Cars, GTSRB, and RESISC45 datasets.

obtained using (Figure 7(h)), there were cases where the proposed method produced better explanations, such as in the GTSRB example shown in the second row of Figure 7.

E Discussion on Computational Complexity of Explanation Generation

As shown in Figure 1, the difference between our self-explaining model, i.e., “prediction-with-explanation” model, and the “prediction-only” model used when generating patch-level attributions with Kernel SHAP is that the former applies the domain-specific head g_W to both the [CLS] token and the M image patches, while the latter applies it only to the [CLS] token. The domain-specific head g_W calculates matrix multiplication $W^T u$ for input feature vector $u \in \mathbb{R}^K$ and weight matrix $W \in \mathbb{R}^{K \times C}$, where C is the number of classes. The computational complexity of this matrix multiplication is $\mathcal{O}(KC)$. Regarding the computational complexity of the feature extractor f_θ as F , the computational complexity of our self-explaining image classifier per explanation is $\mathcal{O}(F + MKC)$ where M is the number of patches in an image. In practice, since MKC is typically much smaller than F , the computational complexity can be approximated as $\mathcal{O}(F)$.

In contrast, the computational complexity of Kernel SHAP per explanation is $\mathcal{O}(PF + PM^2)$, where P is the number of perturbations and PM^2 is associated with solving the least-squares problem. In practice, since PF is much larger than PM^2 , the computational complexity can be approximated as $\mathcal{O}(PF)$.

In summary, the computational complexities of our self-explaining image classifier and Kernel SHAP per explanation are the same asymptotic complexity $\mathcal{O}(F)$ for the feature extractor, but Kernel SHAP has an additional multiplicative factor of P .

F Results on Comparison with Kernel SHAP

Figure 8 shows the explainability scores of the proposed method and Kernel SHAP with varying number of perturbations P when transferring explainability learned on ImageNet+X to the 10 target datasets. For all the scores except IoU@1, the proposed method substantially outperforms Kernel SHAP, even with 1,000 perturbations, demonstrating superior efficiency in generating both accurate attribution values and their rankings. For IoU@1, the proposed method achieves performance equivalent to Kernel SHAP with 300 perturbations, showing particular effectiveness for identifying the most important patch location.

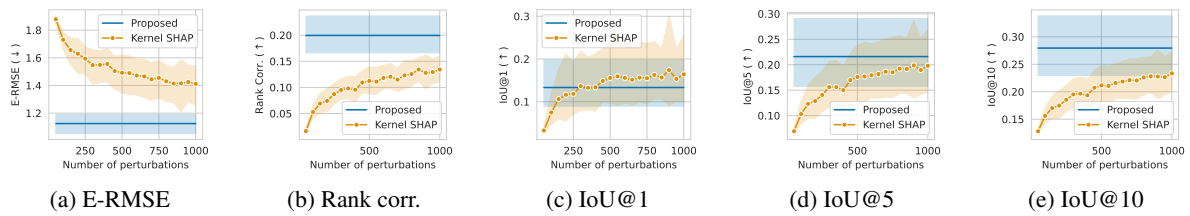


Figure 8: Explainability scores of the proposed method and Kernel SHAP averaged across the target datasets with varying number of perturbations. The shaded area represents the 95% confidence interval.